New insights into aluminosilicate gel from acetic acid attack of hydrated Portland cement: Experimental and thermodynamic characterization

Cédric Roosz, Marie Giroudon, Laurie Lacarrière, Matthieu Peyre Lavigne, Cédric Patapy, Alexandra Bertron

New insights into aluminosilicate gel from acetic acid attack of hydrated Portland cement: experimental and thermodynamic characterization

Cédric Roosz[a], Marie Giroudon[a,b], Laurie Lacarrière[a], Matthieu Peyre Lavigne[b], Cédric Patapy[a], Alexandra Bertron[a]

[a]*LMDC, Université de Toulouse, UPS, INSA, Toulouse, France*
[b]*TBI, Université de Toulouse, CNRS, INRA, INSA, Toulouse, France*

Abstract

Many concrete structures in aqueous environments suffer leaching, affecting their microstructure and durability. The resulting chemical and mineralogical degradation are difficult to predict over the long term and for environments of varying chemical composition, especially for severely degraded cement matrices. This is mainly because of the lack of chemical and thermodynamic data on the degraded phases formed during these attacks. In this context, this study aims to evaluate the chemical changes of leached ordinary Portland cement (OPC) paste by combining experimental (batch experiments) and modelling (thermodynamic equilibria calculations) approaches. The ground OPC paste was gradually added to an acetic acid solution. pH and chemical compositions of the solution were monitored throughout the experiment. The solid fraction was characterised over time, with particular attention paid to the phase obtained during the first additions. The latter was found to be an amorphous aluminosilicate gel (Al/Si = 0.3), with major contributions from Si Q^4 and Al^{IV} (obtained by ^{29}Si and ^{27}Al NMR analyses respectively).

Existing databases (*MINTEQ* 3.0, *Thermoddem*, *Cemdata*) were first used in the thermodynamic simulation of the experiment using PhreeqC, which showed discrepancy with the experiment in the early stages of the attack. They were then improved by the addition of the Si-Al gel identified experimentally. The incorporation of the new phase enabled to better fit the experimental data. The calculated equilibrium constant of the gel at 20 °C ($\log K_{gel}$ = 0.37) was consistent with the equilibrium constants of similar Si-Al phases already explored in the literature.

Keywords: Cement paste, Leaching, Acid attack, Aluminosilicate gel, Solid state NMR, Thermodynamic equilibrium

1. Introduction

Immersed part of strategic concrete structures, such as dams, water supply structures, port infrastructures, pier cap of bridges, are exposed to the action of natural waters (soft water, seawater, groundwater, etc.) in saturated conditions and at close to neutral pH values, resulting in the leaching of the cementitious materials, especially in the case of low salinity waters [1–3]. Moreover, other types of infrastructures can be exposed to even harsher leaching conditions, such as industrial (chemical industries), sewage (sewer pipes and waste water treatment plants [4–6]), or agricultural and/or agro-industrial facilities (manure silos, silage silos, slatted floors in farm buildings, anaerobic digesters, dairy, winery and/or sugar production plants [7–20]) where the pH of the effluents in contact with the concrete is often acidic and can sometimes go down to 1 or 2. These attacks lead to mineralogical and chemical alteration of the concrete, and are accompanied by the increase of porosity and the decrease of concrete alkalinity [21]. The consequences of these attacks on the concrete condition the service life of the structure, and in particular the rate of progression of the deterioration front towards the steel reinforcements [22].

Today, the mechanisms of attack of cementitious matrices, especially those based on Portland cement, by pure and acidic water are relatively well known. These attacks translate themselves into the leaching of calcium in major quantities, but also, other cations of the matrix, and the progressive dissolution of the hydrated phases (C-(A-)S-H, aluminates, etc.) and anhydrous residual grains of the cement matrix. Ultimately the formation of a siliceous or silico-aluminous gel is observed [7,8,23]. Precise description of the mineralogical and chemical evolution of the solid during degradation is hampered by the lack of experimental chemical and mineralogical data on the phases resulting from degradation, in particular the siliceous or silico-aluminous phase, with most of the available data relating to hydrated phases [24–26]. As a result, the silico-aluminous gel observed experimentally is not referenced in any database [24–26] and the current thermodynamic models do not allow the leaching of cementitious matrices to be simulated accurately. Some papers circumvent the problem by using, among others, poorly crystallized zeolites [27] or solid solutions of amorphous silica phases and AH_3 gel [28]. In the latter case, calculations of compositions are carried out with higher Al/Si ratios than in real silicoaluminous gels [29]. Berger et al. [30] recently aimed to

experimentally verify the thermodynamic modelling of cement pastes under acetic acid attack. They highlighted the limitation in the thermodynamic data of the silico-aluminous gel [30].

The aim of this article is to provide some insight into the chemical, mineralogical and thermodynamic characteristics of the Al-Si phases resulting from the leaching of Portland cement-based matrices. Acetic acid was considered as a model chemical compound for generating a strong leaching attack on cementitious materials in order to reach advanced deteriorated states of the cementitious materials leading to the formation of Al-Si gel [21,31]. The aim was (i) to evaluate the chemical reactions between Portland cement matrices and acetic acid, at different solid to liquid ratios until equilibrium, in order to investigate a wide range of deterioration stages of the matrix, and (ii) to complete the thermodynamic data bases of phases formed from leaching.

The study combined batch experiments and PhreeqC thermodynamic simulations, implementing a dialog between both approaches. Grounded hydrated ordinary Portland cement paste was gradually added into a 2 L stirred 0.28 M acetic acid solution (pH ≈ 4) in order to limit diffusion as much as possible, i.e. in such a way that the equilibrium times measured can be explained for the most part by chemical phenomena (without the diffusive aspect within a material). At different stages of degradation, X-ray diffraction and ^{29}Si and ^{27}Al nuclear magnetic resonance were used to analyse cementitious powder and concentrations of cementitious ions were determined using ion chromatography and inductively coupled plasma with optical emission spectrometry. For thermodynamic modelling, several databases were considered: *MINTEQ* 3.00 [26] was used for organic acids and aqueous complexes, *Thermoddem* [25] for formation constants of cement hydrated phases, and *Cemdata* [24] for equilibrium constants of cementitious anhydrous phases. The experimental results have allowed the improvement of the databases by adding and considering in the simulation a new phase identified experimentally.

2. Materials and Methods

2.1. Materials and specimen preparation

Hydrated cement paste of ordinary Portland cement, CEM I 52.5 R (denominated h-CEM I in this paper) was made with a water/cement mass ratio of 0.3. The cement composition, determined by inductively coupled plasma with optical emission spectrometry (ICP-OES) and ion

chromatography, is given in Table 1: Oxide chemical composition of cement h-CEM I 52.5 R (LOI = Loss of ignition). The mixing of pastes was carried out according to a procedure adapted from the standard NF EN 196-1 [32]. The cement paste was cast in cylindrical moulds 70 mm high and 35 mm in diameter. Each mould was sealed and the pastes were removed from their moulds after curing in a tempered room at 20 °C for 28 days. Two specimens were crushed to a particle size of less than 80 µm (using a Restch Type RS100, 15 seconds at 1400 rpm) in order to obtain powder, and were kept in airtight condition until the leaching experiments. The *semi-batch* experiment detailed below was thus duplicated.

Table 1: Oxide chemical composition of cement h-CEM I 52.5 R (LOI = Loss of ignition).

wt.%	**CaO**	**SiO_2**	**Al_2O_3**	**Fe_2O_3**	**MgO**	**TiO_2**	**Na_2O**	**SO_3**	**LOI**
h-CEM I	66.2	20.0	4.85	2.64	1.06	0.27	0.14	3.01	1.64

The solution was made of acetic acid at 280 mmol/L (glacial acetic acid 99.8-100.5%, AnalaR NORMAPUR - VWR) buffered with 50.12 mmol/L of NaOH (sodium hydroxide 98.5-100.5%, AnalaR NORMAPUR - VWR) in order to reach a pH of 3.95.

2.2. Degradation protocols

A protocol was developed to characterize the evolution of the degradation as a function of the solid/liquid (S/L) ratio. The whole protocol is represented in Figure 1 and each experiment is detailed below. It combines two different types of experiments, (*i*) *semi-batch* (Figure 1, process A) and (*ii*) *batch* experiments (Figure 1, process B), depending on the desired characterization, i.e. (*i*) equilibrium solution characterization or (*ii*) solid fraction characterization, respectively.

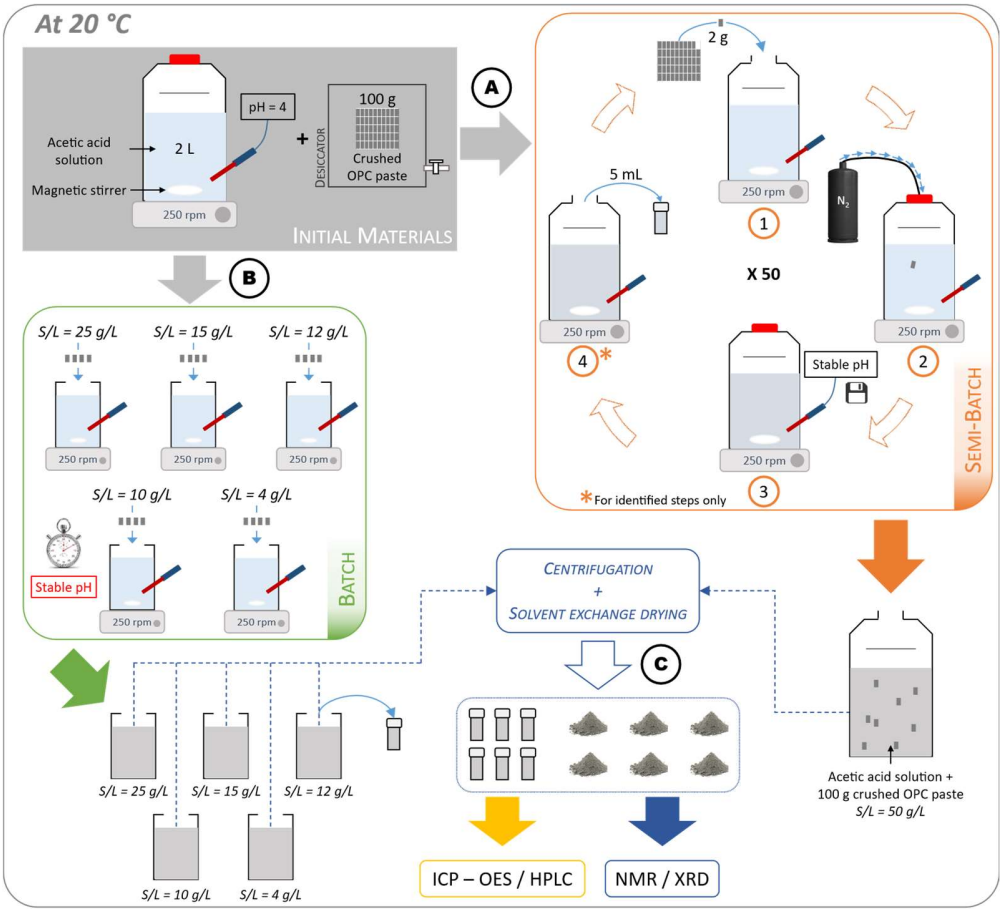

Figure 1: Schematic description of the experimental protocol, consisting exposing crushed h-CEM I paste to acetic acid solution in two types of conditions: (i) semi-batch (process A) *and (ii) batch experiments (process B), intended for the characterization of the (i) equilibrium solution or (ii) solid fraction, respectively (process C).*

2.2.1. Semi-batch experiment

The *semi-batch* experiment consisted in adding, in 50 successive additions of 2 g, a total of 100 g of the powdered h-CEM I paste in 2 L of the acetic acid solution that was constantly stirred (Figure 1-A.1). The reactor was flushed with N_2 after each addition to prevent carbonation of the system (Figure 1-A.2). The pH was monitored continuously and each new addition of powder was made once a stable pH (pH changes lower than 0.01 during 15 min), i.e. chemical equilibrium was reached (Figure 1-A.3). Each addition resulted in an increase of the S/L ratio of 1 g per litre (1 g/L), in such a way that after the last (50^{th}) addition, an S/L ratio of 50 g per litre of degrading solution was reached. The aqueous solution was sampled at different steps for further chemical

analyses (Figure 1-A.4). Finally, the experiment was run twice to ensure repeatability and to refine the results.

At the end of each experiment (i.e. after the last addition) and once the pH was stabilized, the solution was centrifuged to recover the h-CEM I powder (Figure 1-C). This powder was then immersed for 15 minutes in isopropanol for solvent exchange drying [33,34]. After further centrifugation, the powder was recovered and placed in a vacuum desiccator for 1 hour to facilitate solvent removal and complete the drying.

2.2.2. Batch experiments

Since the *semi-batch* experiment does not allow to characterize the evolution of the solid fraction (the unique solid characterisation can be made after the last addition), five *batch* experiments were realized (Figure 1-B), corresponding to different steps (or S/L) of the *semi-batch* process. For that, powdered h-CEM I paste was added in acetic acid solution in order to obtain S/L ratios of 4, 10, 12, 15 and 25 g/L. The solution was mixed and once a stable pH was reached, and the solid was extracted by centrifugation and dried by solvent exchange (Figure 1-C).

2.3. Liquid and solid analyses

The concentrations of calcium, silicon, aluminium, iron and magnesium in the solutions from *semi-batch* and *batch* experiments were determined using ICP–OES [35–37]. The ICP–OES equipment was a Perkin Elmer Optima 7000 DV equipped with a Meinhart nebulizer and a generator power of 1450 W. The flows of argon and air (auxiliary gas) were 15 and 0.2 L/min respectively. The flow at the entry of the nebulizer was 0.6 L/min. Firstly, standards of calcium were prepared at 0.5, 1.0, 5.0, 10.0, 20.0, 50.0, and 100.0 mg/L. Secondly, the solution samples were filtered (0.2 µm filter) and diluted with a factor of 100 (calcium) or 10 (silicon, aluminium, iron and magnesium) in order to fit in the standards concentration range.

The concentrations of sulphate in the solutions were measured using high performance ion chromatography (HPLC) (Dionex ICS-3000). The pre-column and column were respectively a Dionex AG15 and an IonPac AS15. The column flow was of 1.2 mL/min. The gradient of eluent (KOH) was 38 mM and the column temperature was 30 °C. Sulphate standards were prepared between 0.1 and 100 mg/L and the solution samples were diluted ten times.

X-ray diffraction (XRD) patterns of all samples (i.e. powders from batch and semi-batch experiments) were acquired under atmospheric conditions using a Brucker D8 diffractometer equipped with a copper anode (λ $K_{\alpha 1}$ = 1.5406 Å). All scans were performed in continuous scan mode over the 4°-70° 2θ Cu Kα

range. Total counting time was 2.4h, and intensity was integrated every 0.02° 2θ Cu Kα.

Solid-state Nuclear Magnetic Resonance (NMR) analyses of all solid samples were carried out using a Bruker Advance 400 III HD spectrometer operating at magnetic field of 9.4 T. Samples were packed into 4 mm zirconia rotors, spun between 8 to 12 kHz (ν_r) at 295 K. ^{27}Al MAS analyses were performed in a quantitative way with the use of a small flip angle $\alpha < \pi/12$ and a relaxation delay of 1 s. ^{29}Si MAS were acquired with the UDEFT pulse sequence [38] with a recycle delay of 60 s. ^{29}Si CPMAS analyses were performed in a quantitative way with ten 1.1-ms CP periods, 0.9 s ^{1}H recovery time and 1.5 s recycle delay. Chemical shifts were externally referenced to 1 M $Al(H_2O)^{3+}_6$ and TMS solutions, for ^{27}Al and ^{29}Si, respectively. All the spectra were deconvoluted using the Fityk program [39], in individual Gaussian-Lorentzian peaks. This deconvolution used the minimum possible number of component peaks to describe the spectrum accurately, based on information available in the literature for cementitious materials [40–42]. The integration corresponding to the relative amount of the differently coordinated species related to the quantity of considered element in the sample (*Si* or *Al* for ^{29}Si or ^{27}Al acquisitions), proportions of indexed phases were calculated by coupling these NMR data to ICP–OES chemical analyses results through mass balance calculations.

2.4. Modelling approach

2.4.1. Theoretical background and conventions

The mineral-solution equilibria in batch condition depend on all the chemical reactions considered in the system, such as acid/base reactions, ion complexation in solution and dissolution/precipitation of solid phases.

Each reaction allows to constrain the maximum concentrations of its constituting elements in water at a given temperature, i.e. the concentrations corresponding to the thermodynamic equilibrium. This is based on the *law of mass action*, which defines an equilibrium constant, *K*, for each solid phase and aqueous specie, based on reactions of the form $XY \rightleftharpoons X^+ + Y^-$. Considering an equilibrium state at pressure and temperature of reference (P_r and T_r) implies that the ion activity product (*IAP*) reached the value of the equilibrium constant *K* as described in Equation (1), according to the conventions proposed by Helgeson [43].

$$IAP_{XY} = \frac{(X^+) \cdot (Y^-)}{(XY)} = K_{XY}(P_r, T_r) \quad (1)$$

This equation refers to the chemical activities in solution ((X^+), (Y^-)), or *effective concentrations*, which are equal to 1 for solid phases (i.e. if XY is a solid phase, $(XY) = 1$). Considering aqueous species, these activities are obtained by multiplying their molal concentrations (m_{Xi} in mol/kg H_2O) by an activity coefficient (γ_i, dimensionless) as described in Equation (2), where m_{Xi} is related to the molal concentration of ion Xi, and $m^0{}_{Xi}$ the molal concentration of the same ion in the standard state (for aqueous solutions, this refers to an *ideal solution* containing 1 mol/kg of solute undergoing infinite dilution).

$$(Xi) = \gamma_i \cdot \frac{m_{Xi}}{m^0_{Xi}} = \gamma_i . m_{Xi} \quad (2)$$

Although many models have been developed to represent the difference between *real* and *ideal* solutions, the most commonly used model for low concentrated solutions (ionic strength lower than 1 M) is the Debye Hückel model [25,44,45]. The present study is made using PhreeqC software [46], working with the extended Debye-Hückel model B-dot relation described in Equation (3) [43]. This model defines activity coefficients as being function of A and B that correspond to Debye-Hückel parameters, while I refers to ionic strength (Equation (4)), and å and z_i are respectively the ion size parameter (the effective diameter of hydrated ion i, that is empirical) and the charge for species i. At least, $\dot{B}$ stands for the B-dot parameter.

$$log\, \gamma_i = -\frac{A . z_i^2 \sqrt{I}}{1 + \mathring{a}_i . B\sqrt{I}} - \dot{B} I \quad (3)$$

$$I = \frac{1}{2} \sum_i \left(\frac{m_{Xi}}{m^0_{Xi}} . z_i^2 \right) = \frac{1}{2} \sum_i (m_{Xi} . z_i^2) \quad (4)$$

At equilibrium, the resolution of the possible reactions in the studied chemical system leads to a nonlinear system with several couplings between equations by the mean of activities, and considering an electrical balance that tends towards 0. Thus, and for each phase considered, the activity coefficients are calculated and thus the composition of the system at equilibrium.

2.4.2. Thermodynamic data

In these calculations, only main cement ions (Ca, Si, Al, Mg, Na, K, and SO_4) were considered, and iron was neglected. Many iron phases have been described in the literature [24,47–51], but given their compositional variability and considering that these amorphous phases are difficult to characterize experimentally, we could not effectively constrain the model on this aspect.

In order to represent as accurately as possible both the chemical reactions resulting from the degradation of the h-CEM I paste and those involving acetic acid as well as the stability of the main organometallic complexes and organic salts, several databases were implemented.

The *Thermoddem* database [25] was used as "core database", i.e. for the major elements, aqueous species and formation constants of main cement phases. The *MINTEQ* 3.00 database [26] was used for organic acids and aqueous complexes, and *Cemdata* database [24] for equilibrium constants of cementitious anhydrous phases. The different thermodynamic data collected are presented in Table 2 for aqueous species and main cement phases.

The main addition of this work compared to the models proposed by previous studies [52,53] are C-(A-)S-H thermodynamic data recently identified [54]. These data (equilibrium equations and associated solubility constants detailed in Table 3) show ten C/S ratios, from 0.7 to 1.6 and discretized every 0.1, and four different A/S ratios that are 0 (C-S-H), 0.02, 0.05 and 0.1.

Table 2: Thermodynamic equilibrium constants considered for carboxylic calcium salts and cement phases at 25°C

Aqueous species / **Minerals**	Reaction	Log K	Ref.
Acetic acid	$C_2H_4O_2 = CH_3\text{-}COOH$	/	/
H-acetate	$H^+ + C_2H_3O_2^- \leftrightharpoons C_2H_4O_2$	4.76	[26]
Al-acetate^{2+}	$Al^{3+} + C_2H_3O_2^- \leftrightharpoons AlC_2H_3O_2^{2+}$	2.75	[26]
Al-acetate$_2^+$	$Al^{3+} + 2\ C_2H_3O_2^- \leftrightharpoons Al(C_2H_3O_2)_2^+$	4.6	[26]
AlOH-acetate$^+$	$Al^{3+} + C_2H_3O_2^- + H2O \leftrightharpoons AlOHC_2H_3O_2^+ + H^+$	-0.15	[26]
Al$_2$(OH)$_2$-acetate^{3+}	$2Al^{3+} + C_2H_3O_2^- + 2H2O \leftrightharpoons Al_2(OH)_2C_2H_3O_2^{3+} + 2H^+$	-2.41	[26]
Ca-acetate$^+$	$Ca^{2+} + C_2H_3O_2^- \leftrightharpoons CaC_2H_3O_2^+$	1.18	[26]
Ca-(acetate)$_2$	$Ca^{2+} + C_2H_3O_2^- \leftrightharpoons Ca(C_2H_3O_2)2$	2.15	[26]
Ca-(acetate)$_2$(s)[1]	$Ca(C_2H_3O_2)_2(s) \leftrightharpoons Ca^{2+} + 2C_2H_3O_2^-$	-1.9	[26]
SiO_2(am)	$SiO_2 + 2\ H_2O \leftrightharpoons H_4SiO_4$	-2.7	[25]
Portlandite	$CaOH_2 \leftrightharpoons Ca^{2+} + H_2O$	22.81	[25]
Gibbsite	$Al(OH)_3 + 3H^+ \leftrightharpoons 1Al^{3+} + 3H_2O$	7.73	[25]
Ettringite	$Ca_6Al_2(SO_4)_3(OH)_{12}{:}26H_2O + 12H^+ \leftrightharpoons 2Al^{3+} + 6Ca^{2+} + 3SO_4^{2-} + 38H_2O$	57.01	[25]
Monosulfoaluminate	$Ca_4Al_2SO_{10}{:}12H_2O + 12H^+ \leftrightharpoons 2Al^{3+} + 4Ca^{2+} + SO_4^{2-} + 18H_2O$	73.09	[25]
C_3AH_6	$Ca_3Al_2(OH)_{12} + 12H^+ \leftrightharpoons 2Al^{3+} + 3Ca^{2+} + 12H_2O$	80.32	[25]
C_4AH_{13}	$Ca_4Al_2O_7{:}13H_2O + 14H^+ \leftrightharpoons 2Al^{3+} + 4Ca^{2+} + 20H_2O$	103.6	[25]
Hydrotalcite	$Mg_4Al_2O_7{:}10H_2O + 14H^+ \leftrightharpoons 2Al^{3+} + 4Mg^{2+} + 17H_2O$	73.74	[25]
C_2S	$(CaO)_2SiO_2 + 4H^+ \leftrightharpoons 2Ca^{2+} + H_4SiO_4$	38.83	[24]
C_3S	$(CaO)_3SiO_2 + 6H^+ \leftrightharpoons 3Ca^{2+} + H_2O + H_4SiO_4$	73.66	[24]
C_3A	$(CaO)_3Al_2O_3 + 12H^+ \leftrightharpoons 2Al^{3+} + 3Ca^{2+} + 6H_2O$	118.1	[24]
Aluminosilicate gel	$SiAl_{0.31}O_{2.465} + 1.535H_2O + 0.93H^+ \leftrightharpoons 0.31Al^{3+} + H_4SiO_4$	0.37	This work

[1]The symbol (s) is used to discriminate salt from aqueous complex for Ca-(acetate)$_2$

Table 3: Thermodynamic equilibrium constants considered for C-(A-)S-H phases, characterised by their Ca/Si and Al/Si ratios, from Thermoddem database [25] at 25°C

Ca/Si ratio	Al/Si ratio	Reaction	Log K
0.7	0	$Ca_{1.4}Si_2O_{5.95}H_{1.10}$:1.38$H_2O$ + 2.8H^+ + 0.67H_2O ⇋ 1.4Ca^{2+} + 2H_4SiO_4	17.73
0.8	0	$Ca_{1.6}Si_2O_{6.17}H_{1.14}$:1.61$H_2O$ + 3.2H^+ + 0.22H_2O ⇋ 1.6Ca^{2+} + 2H_4SiO_4	21.8
1	0	$Ca_{2.0}Si_2O_{6.64}H_{1.29}$:1.75$H_2O$ + 4.0H^+ ⇋ 2Ca^{2+} + 2H_4SiO_4 + 0.40H_2O	29.46
1.2	0	$Ca_{2.4}Si_2O_{7.12}H_{1.44}$:2.07$H_2O$ + 4.8H^+ ⇋ 2.4Ca^{2+} + 2H_4SiO_4 + 1.19H_2O	37.94
1.4	0	$Ca_{2.8}Si_2O_{7.67}H_{1.77}$:2.23$H_2O$ + 5.6H^+ ⇋ 2.8Ca^{2+} + 2H_4SiO_4 + 1.91H_2O	46.93
1.6	0	$Ca_{3.2}Si_2O_{8.27}H_{2.14}$:2.34$H_2O$ + 6.4H^+ ⇋ 3.2Ca^{2+} + 2H_4SiO_4 + 2.61H_2O	55.94
0.7	0.02	$Ca_{1.4}Al_{0.04}Si_2O_{6.01}H_{1.11}$:1.42$H_2O$ + 2.92H^+ + 0.57H_2O ⇋ 0.04Al3+ + 1.4Ca2+ + 2H4SiO4	17.99
0.8	0.02	$Ca_{1.6}Al_{0.04}Si_2O_{6.23}H_{1.15}$:1.63$H_2O$ + 3.32H^+ + 0.14H_2O ⇋ 0.04Al3+ + 1.6Ca2+ + 2H4SiO4	21.63
1	0.02	$Ca_{2.0}Al_{0.04}Si_2O_{6.71}H_{1.30}$:1.75$H_2O$ + 4.12H^+ ⇋ 0.04Al^{3+} + 2.0Ca^{2+} + 2H_4SiO_4 + 0.47H_2O	29.97
1.2	0.02	$Ca_{2.4}Al_{0.04}Si_2O_{7.18}H_{1.45}$:2.08$H_2O$ + 4.92H^+ ⇋ 0.04Al^{3+} + 2.4Ca^{2+} + 2H_4SiO_4 + 1.26H_2O	38.47
1.4	0.02	$Ca_{2.8}Al_{0.04}Si_2O_{7.75}H_{1.78}$:2.23$H_2O$ + 5.72H^+ ⇋ 0.04Al^{3+} + 2.8Ca^{2+} + 2H_4SiO_4 + 1.98H_2O	47.25
1.5	0.02	$Ca_{3.0}Al_{0.04}Si_2O_{8.04}H_{1.96}$:2.29$H_2O$ + 6.12H^+ ⇋ 0.04Al^{3+} + 3.0Ca^{2+} + 2H_4SiO_4 + 2.33H_2O	51.69
0.7	0.05	$Ca_{1.4}Al_{0.10}Si_2O_{6.11}H_{1.12}$:1.51$H_2O$ + 3.10H^+ + 0.38H_2O ⇋ 0.10Al^{3+} + 1.4Ca^{2+} + 2H_4SiO_4	18.47
0.8	0.05	$Ca_{1.6}Al_{0.10}Si_2O_{6.33}H_{1.16}$:1.67$H_2O$ + 3.50H^+ ⇋ 0.10Al^{3+} + 1.6Ca^{2+} + 2H_4SiO_4 + 0.01H_2O	22.35
1	0.05	$Ca_{2.0}Al_{0.10}Si_2O_{6.81}H_{1.31}$:1.77$H_2O$ + 4.30H^+ ⇋ 0.10Al^{3+} + 2.0Ca^{2+} + 2H_4SiO_4 + 0.58H_2O	30.92
1.2	0.05	$Ca_{2.4}Al_{0.10}Si_2O_{7.28}H_{1.46}$:2.11$H_2O$ + 5.10H^+ ⇋ 0.10Al^{3+} + 2.4Ca^{2+} + 2H_4SiO_4 + 1.39H_2O	39.46
1.4	0.05	$Ca_{2.8}Al_{0.10}Si_2O_{7.85}H_{1.79}$:2.23$H_2O$ + 5.90H^+ ⇋ 0.10Al^{3+} + 2.8Ca^{2+} + 2H_4SiO_4 + 2.08H_2O	48.41
1.5	0.05	$Ca_{3.0}Al_{0.10}Si_2O_{8.13}H_{1.96}$:2.29$H_2O$ + 6.30H^+ ⇋ 0.10Al^{3+} + 3.0Ca^{2+} + 2H_4SiO_4 + 2.42H_2O	52.89
0.7	0.1	$Ca_{1.4}Al_{0.20}Si_2O_{6.27}H_{1.13}$:1.70$H_2O$ + 3.40H^+ + 0.04H_2O ⇋ 0.20Al^{3+} + 1.4Ca^{2+} + 2H_4SiO_4	19.9
0.8	0.1	$Ca_{1.6}Al_{0.20}Si_2O_{6.49}H_{1.18}$:1.76$H_2O$ + 3.80H^+ ⇋ 0.20Al^{3+} + 1.6Ca^{2+} + 2H_4SiO_4 + 0.26H_2O	23.76
1	0.1	$Ca_{2.0}Al_{0.20}Si_2O_{6.96}H_{1.33}$:1.80$H_2O$ + 4.60H^+ ⇋ 0.20Al^{3+} + 2.0Ca^{2+} + 2H_4SiO_4 + 0.77H_2O	33.09
1.2	0.1	$Ca_{2.4}Al_{0.20}Si_2O_{7.44}H_{1.48}$:2.16$H_2O$ + 5.40H^+ ⇋ 0.20Al^{3+} + 2.4Ca^{2+} + 2H_4SiO_4 + 1.60H_2O	42.3
1.4	0.1	$Ca_{2.8}Al_{0.20}Si_2O_{8.01}H_{1.81}$:2.24$H_2O$ + 6.20H^+ ⇋ 0.20Al^{3+} + 2.8Ca^{2+} + 2H_4SiO_4 + 2.25H_2O	52.19
1.5	0.1	$Ca_{3.0}Al_{0.20}Si_2O_{8.29}H_{1.97}$:2.29$H_2O$ + 6.60H^+ ⇋ 0.20Al^{3+} + 3.0Ca^{2+} + 2H_4SiO_4 + 2.58H_2O	57.11

Figure 2 presents simplified stability diagrams of (*i*) calcium salts and conjugated bases (Figure 2-A), and (*ii*) synthetic C-S-H from *Thermoddem* database [25], with respect to pH. These phase diagrams are used to determine the aqueous species and solid phases that are stable when the pH or the acid concentration evolves. The activity approximately corresponds to the concentration for activity ≤ 5.10^{-2}. Above this value, activity corrections would be required. In addition, only the predominant species (with maximum activity) are represented on these diagrams.

Figure 2-A shows that the use of these C-(A-)S-H equilibrium constants are in good agreement with the observations made by previous studies [53], with regard to the stability of the $Ca(Acetate)_2(aq)$. Figure 2-B highlights the evolution of the stability domains of the with different C/S ratios.

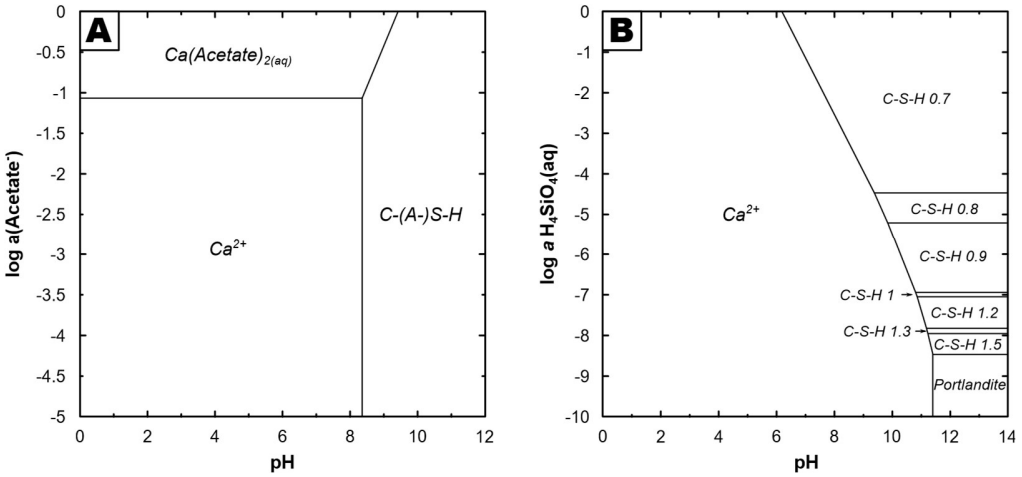

Figure 2: Simplified speciation predominance diagrams of calcium with respect to pH and activity of acetate (A) or H4SiO4 (B)

2.4.3. Modelling procedures

Numerically, and considering the number of equations of this non-linear system (about sixty equations for as many unknowns), the whole calculation is solved by a Newton-Raphson method based on the residuals of each equation and the associated Jacobian matrix (expressed with respect to the considered unknowns). This numerical resolution is integrated into PhreeqC [55] and has been widely proven in many fields.

The equilibrium calculations were made using the initial solid composition of anhydrous cement (from Table 1) and the acid solution described above.

In order to simulate semi-batch experiments, 50 calculations have been carried out, according to the different S/L ratios (from 1/1000 to 50/1000). Each step was calculated at the chemical equilibrium.

3. Experimental characterizations

3.1. Solution compositions

Solution compositions and pH of extracted liquid samples from batch and semi-batch experiments are presented as a function of the S/L ratio of the system, in Figure 3. As a reminder, each addition of h-CEM I paste powder corresponds to an increase in the S/L ratio of 1 g/L.

Four main stages can be observed in the evolution of pH values and ion concentrations in solutions. The pH (Figure 3-A) increased from 3.95 in the initial acetic acid solution to 12.1 after equilibration with the last powder addition (i.e. for an S/L ratio of 50 g/L). The first stage (*I*), from 1 g/L to 11 g/L, is showing an increase of pH values from 4 to 5.5, corresponding to the buffer zone of the acetic acid where high release of hydroxide ions leads to moderate increase of the pH [56]. The second one (*II*), between 12 g/L and 17 g/L, shows an increase of pH from 5.8 to 11.3, corresponding to the neutralization zone of the acid where high pH rise is observed for small release of hydroxide ions. Then this increase slows down until 27 g/L (*III*), and the pH values seem buffered around 12.1 after this point (*IV*).

Considering ion concentrations, the same stages can be observed. During the first stage (*I*) a linear increase of all analysed elements, i.e. proportional to the quantity of added powder, is noticed (dotted lines). Si, Al and Fe concentrations show a maximum after 8 g/L (Figure 3-C) with values around 10, 2.5 and 1 mmol/L, respectively, and then a decrease of the ion concentrations. This reflects the precipitation of Si-, Al- and Fe-rich phases after this addition, probably amorphous gels since the pH of the equilibrated solution is below 6. During stage (*II*), the increase of Ca, Mg and SO_4 concentrations slows down (Figure 3-B and Figure 3-D). Then, calcium concentration stabilizes around 120-130 mmol/L from 15 g/L, while SO_4 concentration reaches a maximum around 2.2 mmol/L after 11 g/L, and Mg concentration shows a maximum around 5 mmol/L at an S/L ratio of 17 g/L. Considering Si, Al and Fe concentrations, they show a sharp decrease, and are close to 0 after 17 g/L. This evolution could correspond to the precipitation of the main cementitious hydrates such as C-(A-)S-H among others. During stage (*III*), a slight decrease is observed for calcium concentrations, while Mg and SO_4 concentrations drop sharply, revealing precipitation of magnesium- and

sulphate-rich phases. Finally, in stage (IV), calcium concentrations remain stable, while the concentrations of the other elements are close to 0. This last evolution, associated with the constant pH of 12.1 of the equilibrium solution, could correspond to the precipitation of portlandite, acting as a buffer [57,58]. Finally, potassium concentrations increase almost linearly along the experiment.

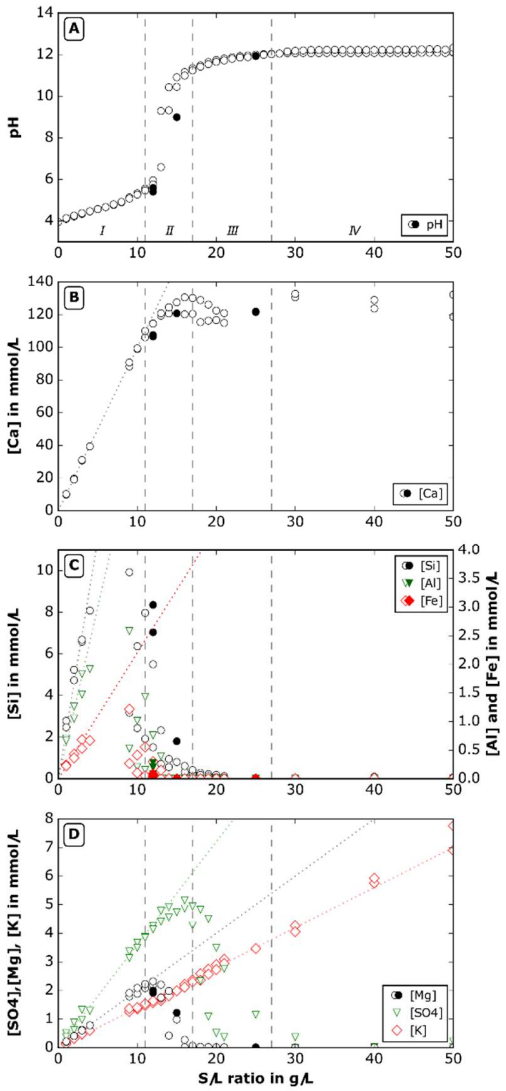

Figure 3: Experimental pH values (A), and calcium (B), silicon, aluminium and iron (C), sulphate and magnesium (C) concentrations in equilibrium solutions for each step of powder addition in the semi-batch (empty symbols) and batch experiments (filled symbols). B, C and D X-axis are broken between 30 and 50 g/L to ease reading, and dotted plots are corresponding to a theoretical total dissolution of the h-CEM I paste. [SO_4] and [K] were not measured for the batch experiment.

Considering the composition of the h-CEM I cement (Table 1), the quantities of analysed elements were close to the quantities entered in the system for the first additions (*I*) (dotted plots in Figure 3 represent the hypothetical concentrations in solution resulting from a total dissolution of the solid added). This shows that the chemical equilibrium was almost reached for the first steps, regardless of iron. In fact, the measured concentrations of iron represented only 70% of the iron added in the system. Moreover, the part of dissolved iron decreases rapidly and only represents 50% of the iron entered into the system after the third addition. This could be due to the low reactivity of C_4AF [59–61], especially at alkaline pH. The dissolution rate of C_4AF would therefore decrease as the pH of the equilibrium solution rises.

All these chemical observations are consistent with previous works on the degradation of cementitious materials by organic acids. In these studies, mechanisms involving mineralogical transformations driven by the decalcification of the cement paste were detailed [8,20,31,62].

3.2. XRD analyses

XRD analyses were performed on powdered h-CEM I, as well as on the solid samples from batch experiments at S/L ratios of 12 g/L, 15 g/L and 50 g/L. The results are shown in Figure 4. It should be considered that these results are not quantitative, and the vertical scales of the different samples are not comparable. Unaltered h-CEM I powder pattern shows the typical phases encountered in CEM I paste, such as anhydrous (C_2S, C_3S, C_4AF) and hydrated (C-S-H, ettringite, portlandite, hemicarbonate, hydrotalcite) phases.

The diffractograms of degraded samples first show an important dissolution of the hydrated phases (12 g/L), associated with a broad diffraction band centred between 26-27° 2θ related to amorphous silica [63–65]. For this sample, almost all hydrates seem to be dissolved and only anhydrous phases as C_4AF remain. The comparison between 12 g/L and 15 g/L diffractograms only shows that calcite precipitated at 15 g/L, which can be due to an experimental effect (carbonation due to air exposure during sample filtration). The last sample (50 g/L) diffractogram shows the presence of a significant amount of hydrates such as ettringite, hemicarbonate, portlandite, as well as C-S-H with a broad diffraction band centred around 30-32° 2θ [63,65–67]. This diffractogram is still different from that of the unaltered h-CEM I sample, with the presence of hydrotalcite, quartz and calcite, and a broad diffraction band centred around 30-32° 2θ showing the more amorphous nature of the sample.

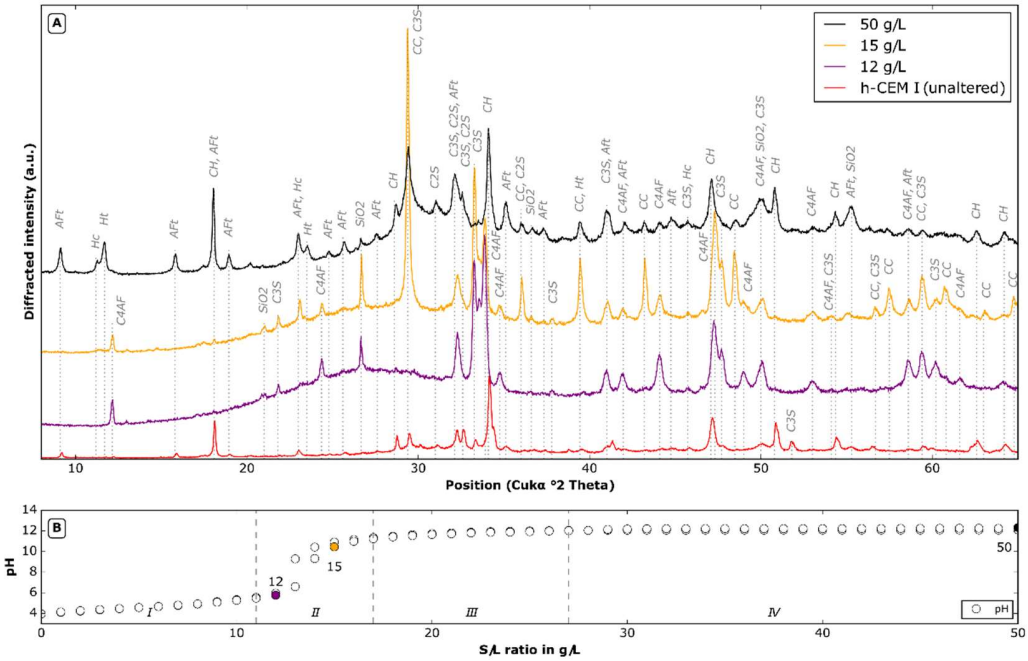

Figure 4: XRD patterns corresponding to initial hydrated CEM I powder, and 12, 15 and 50th additions of the batch experiments (A), related to the pH of their equilibrium solutions (B). AFt: Ettringite, C2S: Belite, C3S: Alite, C4AF: Brownmillerite, CC: Calcite, CH: Portlandite, Hc: Hemicarbonate, Ht: Hydrotalcite, SiO2: Quartz.

3.3. Solid state NMR measurements

NMR analyses were carried out on the unaltered h-CEM I powder as well as on the remaining powders (*i*) filtered at the end of the semi-batch experiment (S/L ratio of 50 g/L) and (*ii*) from the batch experiments (S/L of 4, 10, 12, 15 and 25 g/L).

The results of ^{29}Si NMR measurements are reported on Figure 5-A, and the quantifications calculated from the deconvolution of the spectra are summarized in Table 4. ^{29}Si NMR spectra being normalized according to their chemical composition, the total area under each curve corresponds to the silica content of the solid sample (calculated by mass balance from the chemical compositions of the corresponding equilibrium solution). Unaltered h-CEM I powder shows strong contributions of Q^1 and Q^2 (from -79 to -90 ppm) that are attributed to C-S-H with high C/S ratios (Q^1/Q^2 ratio higher than 1), these contributions represent 48.5% of the signal [63,68]. Q^0 contribution (between -65 and -75 ppm) is often attributed to C_2S and C_3S anhydrous phases and correspond to 30% of the signal, i.e. of the total silicon in the solid. Samples from batch experiments with S/L of 4, 10, 12 and 15 g/L show only one large Q^4 contribution, showing that silicon is present in one amorphous phase that could correspond to amorphous silica. The 25 g/L sample shows the presence

of 64% of Q^1 and Q^2 (between -79 and -90 ppm) that can be attributed to C-S-H that have lower C/S ratio than in unaltered h-CEM I powder (Q^1/Q^2 ratio less than 1). Q^0 contribution, attributed to anhydrous phases (C_2S, C_3S) represents 17.7% of the signal, and Q^3/Q^4 contribution, corresponding to amorphous silica, represents about 18.4% of the signal. The 50 g/L sample (i.e. powder after the last addition of the semi-batch experiment) shows 72.4% of C-S-H with high C/S (Q^1/Q^2 ratio similar to those observed on unaltered h-CEM I) with 13.3% of anhydrous phases and 14.4% of amorphous silica.

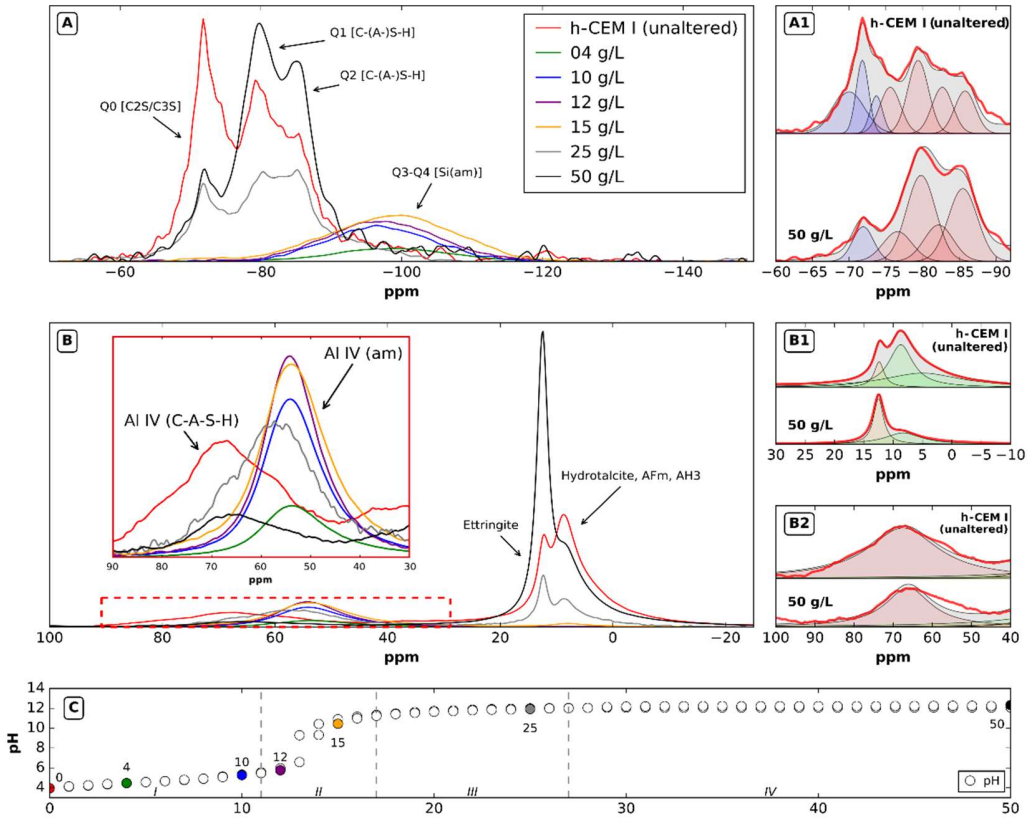

Figure 5: ^{29}Si (A) and ^{27}Al (B) NMR spectra of initial h-CEM I powder and solid sampled from batch experiments at S/L ratios of 4, 10, 12, 15, 25 and 50 g/L, with corresponding pH values of their equilibrium solutions (C). All spectra are normalized according to their chemical composition (see text).

Table 4: Position and population of ^{29}Si NMR environments identified for each sampled step, related to deconvolution of NMR spectra.

Sample	Q^0 (%) *-65/-75 ppm*	Q^1 (%) *-79/-80 ppm*	Q^2 (%) *-82/-86 ppm*	Q^3/Q^4 (%) *-90/-110 ppm*
Powdered h-CEM I paste	30	27.8	20.7	21.5
04 g/L				100
10 g/L				100
12 g/L				100
15 g/L	2	0.3	2.6	95.1
25 g/L	17.7	34.4	29.6	18.3
50 g/L	13.3	37.3	35.1	14.3

Table 5: Position and population of ^{27}Al NMR environments identified for each sampled step, related to deconvolution of NMR spectra.

	Al^{IV} (%)		Al^{V} (%)	Al^{VI} (%)			
	68/57	*55*	*35.5*	*12.4*	*8.7/7.5*	*5*	*-2*
Sample	*ppm*	*ppm*	*ppm*	*ppm*	*ppm*	*ppm*	*ppm*
Powdered h-CEM I paste	23	-	1.7	8	33	34.3	-
04 g/L	-	85.6	-	-	-	-	14.4
10 g/L	-	99.1	-	-	-	-	1
12 g/L	-	98.9	-	-	-	-	1.1
15 g/L	-	94.3	-	-	5.7	-	--
25 g/L	54.9	-	-	11.3	33.8	-	-
50 g/L	5.4	-	0.8	49.3	44.6	-	-

The results of ^{27}Al NMR measurements are reported on Figure 5-B and the related quantifications calculated from the deconvolution of the spectra are summarized in Table 5. ^{27}Al NMR spectra are also normalized according to their mass content of aluminium, meaning that the total area under each curve corresponds to the calculated aluminium content of the sample (calculated by mass balance from the chemical compositions of the corresponding equilibrium solution). Unaltered h-CEM I powder shows strong contributions corresponding to Al^{VI} between 3 and 9 ppm (67.3% of the signal), that can be attributed to hydrotalcite, AFm and gibbsite (AH_3) (Table 5) [69,70]. By contrast, contributions attributed to C-A-S-H (Al^{IV} between 40 and 90 ppm) and ettringite (Al^{VI} between 10 and 12 ppm) represent respectively 23% and 8% of the signal, i.e. the aluminium content. Samples from batch experiments with S/L ratios of 4, 10, 12 and 15 g/L are showing only one contribution of

Al^{IV} centred around 50 ppm that can be attributed to an amorphous aluminous gel. The 25 and 50 g/L samples show the progressive precipitation of ettringite, aluminates and C-A-S-H.

These NMR results are coherent with X-ray diffractograms, with a higher ratio of amorphous/hydrates in the sample equilibrated at 50 g/L than in the unaltered h-CEM I powder. Moreover, C-(A-)S-H have quite similar C/S ratios (i.e. Q^1/Q^2 ratios on ^{29}Si NMR spectra) in this last sample compared to unaltered h-CEM I powder, which seems logical since portlandite is present in solid sampled after 50 g/L, and the C-(A-)S-H are in equilibrium with such high calcium concentrations. In addition, the quantities of anhydrous phases (C_2S and C_3S on ^{29}Si NMR spectra) seem lower in the most altered sample (S/L = 50 g/L) that in the unaltered sample (i.e. solid before experiment). This seems to be in line with the observations made on the X-ray diffractograms, as higher proportion of amorphous and hydrates can be seen for this last sample (broad diffraction band centred around 30-32° 2θ). Finally, we could consider the presence of a unique aluminosilicate gel that is stable for S/L below 15 g/L since the evolution of the Q^4 contribution's area observed in ^{29}Si is similar to that observed at 50 ppm on ^{27}Al, the latter does not appear to be related to any cementitious phase documented in the literature.

4. Discussion of experimental evidences through thermodynamic simulations

4.1 Thermodynamic simulation with existing databases

A first equilibrium model was realized on the basis of published thermodynamic data described in Tables 2 and 3 and compared with aqueous measurements. The results of these calculations are presented in Figure 6-A, Figure 6-B, Figure 6-C for solutions compositions and in Figure 6-D for corresponding solid proportions.

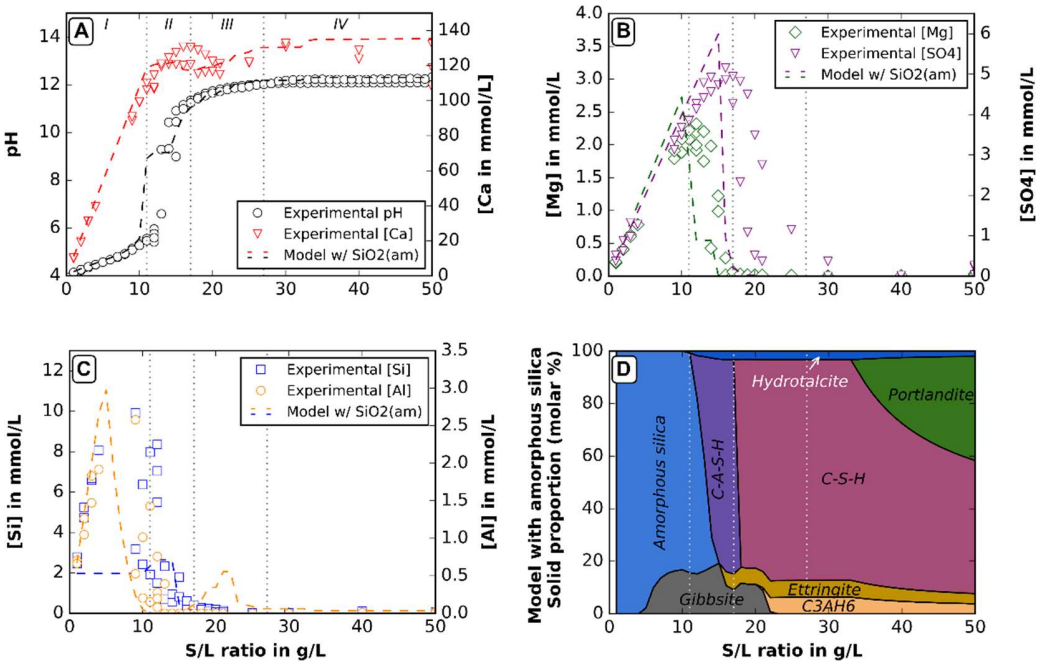

Figure 6: Calculated solutions compositions, with regard to experimental data, and solid fractions: (A) pH values and calcium concentrations, (B) magnesium and sulphate concentrations, (C) silicon and aluminium concentrations, and (D) solid phases.

Experimental data acquired on solutions are fairly well reproduced by the simulation for the main element in solution (calcium).

The evolution of Ca concentration is closely linked to the dissolution-precipitation of cement phases. A linear increase of calcium in solution until S/L = 11 g/L is observed, and is due to the complete dissolution of the added grounded hydrated cement. It is consistent with the results presented in Figure 6-D showing that no solid phases precipitates at these ratios.

From S/L = 11 g/L, the Ca concentration does not follow the linear evolution that would be obtained if all the calcium content in the added solid was in solution. This is related to the progressive precipitation of C-A-S-H and C-S-H, and to a lesser extent ettringite and C_3AH_6 from S/L = 16 g/L and 22 g/L). For this S/L, the C-A-S-H composition is calculated with Al/Si = 0.05 and Ca/Si = 0.7 (these calculated ratios are evolving pretty linearly to reach Al/Si = 0 at step 19 and Ca/Si = 1.6 at step 33, i.e. equilibrated with portlandite).

After S/L = 27 g/L a stabilization of the calcium concentration is observed near 135 mmol/L. It is worth noticing that for this environment (presence of CH_3COO^- from the acetic acid at 0.28M) the solid phases of the "sound" cement paste (between S/L = 40 and 50 g/L the solid phases precipitating in the

solution are similar to sound paste phases) are equilibrated with a much higher calcium concentration than the usual interstitial solution in hydrated cement paste (around 20-22 mmol/L [71]). This can be explained by the fact that the electroneutrality of the solution imposed a high cation concentration to equilibrate the anions brought by acetic acid. Similar results were found in presence of other salts (NaCl, $CaCl_2$, etc.)[72].

These results shed light on the leaching mechanisms by an acid for which the intensity of the attack is not only controlled by the concentration of the hydronium ion but also by the presence of a counter-ion (anion). This one, by its disturbance of the electroneutrality of the solution, changes the equilibrium of cement phases (mainly calcic). This type of mechanism is likely to play a role of calcium pump in the cement materials.

For minor phases, it can first be observed that the model also fits quite well the experimental results for Mg and SO_4. The precipitation of associated solid phases (hydrotalcite and ettringite) is slightly anticipated in the model (occurring respectively at S/L = 11 and 16 g/L). This could be explained by:

- The fact that each step modelled assumes that thermodynamic equilibrium is reached (kinetics not considered). In the experiments, the solution is sampled for concentration measurements when the pH is considered stable for 15 min (i.e. when pH change is lower than 0.01). This observation based on pH evolution does not ensure that equilibrium has been fully achieved.
- Possible uncertainties in solubility data of hydrotalcite and ettringite (equilibrium constant and/or stoichiometry)

Concerning Si concentrations, the model fits the results for S/L ≥ 11 g/L. From this concentration, the simulations show that C-A-S-H precipitate, so that the Si concentration is mainly driven by these phases, whose precipitation is well reproduced by the model as already discussed for Ca concentration.

For low S/L ratios, the model highly underestimates the Si concentration remaining in solution. In this simulation, precipitation of amorphous silica is predicted because, according the database used, this phase is stable under these chemical conditions. On the contrary, experimental results show that, up to approximately S/L = 4 g/L, the Si concentration follows a linear evolution corresponding to a total dissolution of added Si, without any re-precipitation of Si-rich solid phases.

This poor simulation of experimental results for low S/L ratios is also partly observed for Al concentration, for which, to a lesser degree, the model predicts precipitation for lower S/L. Indeed, simulation predicts the precipitation of

gibbsite from S/L = 4 g/L, which is in contradiction with ^{27}Al NMR results, that does not show any Al^{VI} band. This evolution of calculated aluminium concentrations is mainly due to the fact that this equilibrium model lacks stable alumina phases at low pH. Thus, a decrease in gibbsite stability (using, for example, an amorphous AH_3 present in *Thermoddem* or *Cemdata* databases) would result in a very significant overestimation of aluminium concentrations. On the contrary, a reduced stability of C_3AH_6 would have virtually no impact on calculated concentrations, as it would be replaced by monosulfoaluminate, precipitating sulphur at the detriment of ettringite. Some of the aluminium would then be incorporated into C-A-S-H.

All this highlights that the solubility data (equilibrium constant and stoichiometry) of the possible stable phases at these chemical conditions (low S/L ratios and low pH) are poorly estimated by the current thermodynamic database. Moreover, in the experiments the evolution of Al concentration exhibits the same trend as the Si one. This can suggest a correlated precipitation of Si- and Al-rich phase(s), which is not the case in the simulation. This type of correlation, suggesting the precipitation of a silico-aluminous gel, has already been documented in previous works [73] In recent years, a great deal of work has been carried out on such gels [24,74,75], tending to incorporate sodium and potassium. However, the evolution of concentrations measured in our study does not allow us to assert that this is the case here, or only in very small proportions.

4.2 Improvement of databases for alumino-silicate gel in acid conditions

For ^{29}Si-NMR a unique signal is present for low S/L ratios (Figure 5-A) centred on Q^3/Q^4 bands (known as amorphous silica band). For these same ratios, ^{27}Al-NMR has also shown a unique broad signal centred on band at 55 ppm, that indicates the amorphous nature of the Al-rich phase present. This aluminium has a tetrahedral coordination, that is close to the structure of the amorphous silica.

Based on these two experimental findings, it can be assumed that the solid phases at low S/L ratios (until at least 10 g/L) have precipitated as a unique amorphous Si-Al-rich phase. These could also explain the correlation in Si and Al concentrations evolutions in solution observed until S/L = 15 g/L.

In order to determinate the chemical composition of this aluminosilicate gel, mass balance calculation has been used from measured solution concentrations. Knowing the quantity of h-CEM I powder added and the chemical composition of both powdered h-CEM I and equilibrated solution, an

estimation of the solid phases chemical composition can be made as proposed by Equation (5):

$$n_{i_{ps}} = C_{m\,i_{added\ CEMI}} \cdot m_{added\ CEMI} - [i]_{ICP} \cdot V_{batch\ solution} \quad (5)$$

Where:

- $n_{i_{ps}}$ is the quantity of element I (Si or Al) present in the precipitated solid [mol]
- $C_{m\,i_{added\ CEMI}}$ is the molar quantity of element i per mass of hydrated CEMI (issued from table 1) [mol/g]
- $m_{added\ CEMI}$ is the mass added at the considered step [g]
- $[i]_{ICP}$ is the concentration of element i in solution measured by ICP-OES (see Figure 3) [mol/L]
- $V_{batch\ solution}$ is the volume of the batch solution (2L in these experiments) [L]

For S/L ratio equal to 10 g/L, Table 4 and Table 5 show that both Si and Al are entirely present in a unique solid phase that, as explained before, can be considered as an aluminosilicate gel. Equation (6) allows evaluating the stoichiometry of this newly formed phase at these chemical conditions (low S/L ratio and low pH).

$$\frac{A}{S}_{gel} = \frac{n_{Al_{ps}}(10g/L)}{n_{Si_{ps}}(10g/L)} = 0.3 \quad (6)$$

If the same approach is applied on other low S/L ratios (4 and 12 g/L) exhibiting also a unique solid phase, the same A/S ratio can be found. It should be noticed that, due to experimental and deconvolution uncertainties, the A/S ratio is evaluated with only one significant digit.

At slightly higher S/L ratio (15 g/L) NMR results (Table 4 and Table 5) show that other solid phases also precipitate (mainly C-A-S-H). The amorphous phase represents 95% of Si signal and 94% of Al signal. For this ratio, the A/S ratio of aluminosilicate gel can also be estimated on the amorphous phase proportion as following, the result being the same as above (one significant digit):

$$\frac{A}{S}_{gel} = \frac{0.94 \cdot n_{Al_{ps}}(15g/L)}{0.95 \cdot n_{Si_{ps}}(15g/L)} = 0.3 \quad (7)$$

The reaction equation of this gel formation/dissolution can thus be written as follows:

$$0.3\ Al^{3+} + H_4SiO_4 \leftrightarrows Al_{0.3}SiO_{2.45} + 1.55H_2O + 0.9\ H^+ \quad (8)$$

Considering that the solution has been analysed at equilibrium, the equilibrium constant of this new Al-Si-rich phase can thus be evaluated from the reaction quotient, or ionic activity product ($Q = K$ at equilibrium), as detailed in Equation (1) (at P_{atm} and 25°C).

$$\log K_{A-S\ gel} = \log IAP_{A-S\ gel} = \log\left(\frac{(Al^{3+})^{0.3} \cdot (H_4SiO_4)}{(H^+)^{0.9}}\right) = 0.37 \quad (9)$$

The activities (Al^{3+}) and (H_4SiO_4) are evaluated using PhreeqC from Al and Si measured concentrations in solution and the solution speciation.

The identified equilibrium constant can be compared with the existing data for other mineral phases containing Al and Si associated with other elements such as Na and/or Ca (crystalline zeolites stable below 150°C, from *Thermoddem* [25] and *Cemdata* [24] databases), as illustrated on Figure 7 (grey marks for zeolite, red one for Al-Si gel of this study). The results (for phases able to precipitate at ambient pressure and temperature and for similar Si and Al proportion) give similar equilibrium constant as the one identified in this study. But it should be noted that the use of these mineral phases also containing Ca and/or Na would influence stoichiometry calculation and, in the case of the degradation of cementitious materials, would distort the calculation of calcium concentrations in solution and therefore that of the other calcium phases. In addition, it should be noted that the zeolites close to our gel are the most silica-rich zeolites, and therefore those whose silica tetrahedron rings are the most polymerized (i.e. structurally closest to what we would expect from a silico-aluminous gel). Logically, zeolites with high Al/Si ratios do not follow the same trend, since their structure is fundamentally different, and they have significant calcium and sodium contents [76,77].

In this figure, green square marks correspond to pure silica and alumina poles (amorphous silica, quartz, gibbsite) and the dotted line represents a possible solid solution between amorphous silica and amorphous $Al(OH)_3$. This seems to show that it would also be possible, at least in the case of low proportions of aluminium, to model these aluminosilicate gels by a Si(am)-$Al(OH)_3$(am) solid solution.

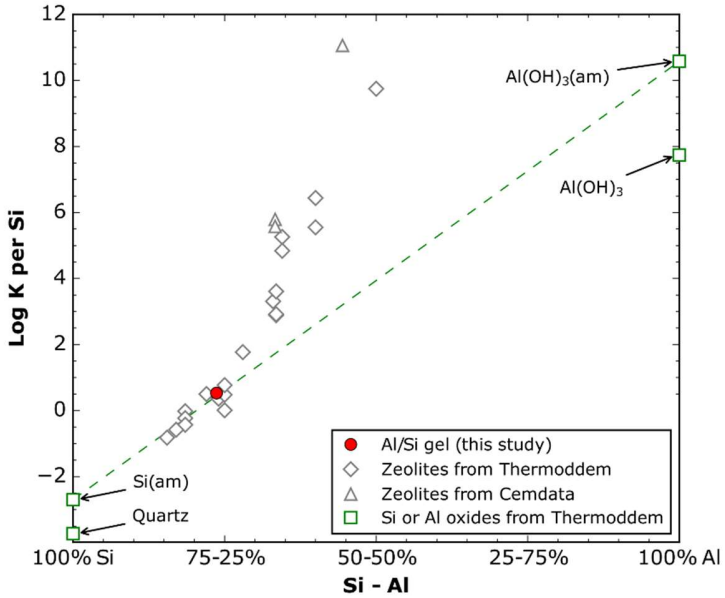

Figure 7: Equilibrium constant for Al-Si rich phases that can precipitate at 25°C and P_{atm} (pure silica and alumina poles in green and zeolites in grey) issued from Thermoddem database [25] compared with the Al-Si gel identified in this study (in red)

4.3 Thermodynamic simulation with newly defined aluminosilicate gel

A new simulation of semi-batch experiments has been conducted including the acquired data on aluminosilicate gel. The results of this new simulation are presented in Figure 8 (A, B and C for solutions compositions and D for corresponding solid proportions).

The results of this second simulation are quite close to the previous one for the pH values and the concentrations of calcium and sulphate (Figure 8 A and B). The most important changes are visible at low S/L ratios, for silica, aluminium and magnesium concentrations (Figure 8 C and D).

In the case of silica, the evolution of calculated concentrations shows a linear increase between the first addition (~ 3 mmol/L) and the S/L ratio of 4, where these concentrations reach a maximum of 12 mmol/L. The concentrations then plateau between 10 and 12 mol/L between S/L ratios 4 and 12, which is roughly consistent with the experimental values. Finally, the concentrations decrease linearly between S/L 12 and 15. The experimental data are thus better reproduced by the model, in terms of trends and orders of magnitude, even if a discrepancy is observed.

For aluminium, the calculated concentrations increase linearly between 2 and 8 mmol/L for S/L ratios of 1 to 4 respectively. They then decrease linearly until reaching values close to 0 for an S/L ratio of 10.

The new proposed aluminosilicate gel has been added in calculations, resulting in silicon and aluminium concentrations closer to the experimental values (Figure 8-D).

There is however a slight overestimation of the concentrations between the 10th and the 20th additions, mainly due to the competition between the aluminosilicate gel and the C-A-S-H. With regard to aluminium concentrations, the trend is similar to the that of the model without aluminosilicate gel but with a lower maximum value. This could be due to a change in the Al/Si ratio of the aluminosilicate gel, which was not estimated experimentally here. The use of C-A-S-H with higher Al/Si ratios, and the consideration of kinetics, would enable a better representation of the experimental data on this point.

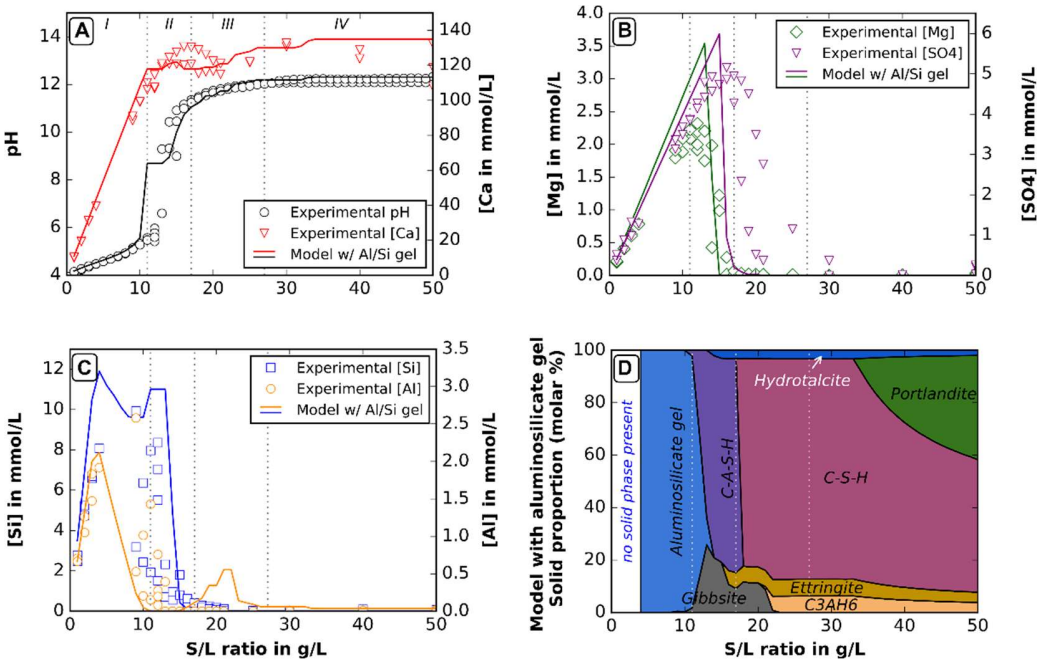

Figure 8: Calculated solutions compositions, with regard to experimental data, and solid fractions (model with alumino-silicate gel): (A) pH values and calcium concentrations, (B) magnesium and sulphate concentrations, (C) silicon and aluminium concentrations, and (D) solid phases

The numerical results obtained for solid phases (Figure 8D) show that no solid phase is stable for S/L ratios of less than 4 g/L. This is consistent with the ICP-OES measurements, since all the elements introduced via the dissolution of the ground cement paste are found in the quantities of elements measured

in solution up to an S/L ratio of 4 g/L. At S/L ratios between 4 and 10 g/L, the precipitation of an aluminosilicate gel can be observed, which delays the precipitation of gibbsite. Concerning calculated C-A-S-H compositions, the results are close to the model with amorphous silica, as calculated ratios at S/L = 11 are 0.05 for Al/Si and 0.7 for Ca/Si (with the same evolution increasing S/L ratio).

Above an S/L ratio of 12g/L the results are similar to those obtained with the initial database. The good adequacy of the solid results is therefore confirmed with the XRD observations, i.e. no hydrated crystallised phases (ettringite, CH) present at S/L of 12 and 15 g/L.

5. Conclusions

In this study, a semi-batch experiment was elaborated consisting of the gradual addition of powdered OPC paste to an aggressive acetic acid solution in order to limit the effect of diffusion inside of materials as much as possible, so as to be comparable with thermodynamic equilibrium calculations. In the first instance, the use of existing thermodynamic databases enabled the measured chemical composition evolution of the liquid to be represented fairly well, except for the Si and Al data at low pH (low solid/liquid ratios), highlighting a lack of data (equilibrium constants, phases) in these low pH conditions. While only amorphous silica and gibbsite precipitated at low S/L ratios using existing databases, ^{29}Si and ^{27}Al NMR analyses of the solid revealed the presence of an aluminosilicate gel, a phase that is not included in any existing database. A composition (solid characterization) and an equilibrium constant (from chemical analyses and modelling) were proposed for this aluminosilicate gel stable at low pH and were in agreement with existing data of Al- and/or Si-rich phases (zeolites, $Al(OH)_{3(am)}$ and $SiO_{2(am)}$).

Finally, these various analyses and calculations have made it possible to add a new phase, identified experimentally, to the considered thermodynamic databases, and to considerably improve the fit of experimental data.

5. Acknowledgements

Financial support was provided by the French National Research Agency (A.N.R.) for funding the project BIBENdOM - ANR - 16 - CE22 - 001 DS0602. The authors also thank Y. Coppel (LCC-CNRS laboratory - UPR 8241) for NMR measurements.

References

[1] M. Rosenqvist, A. Bertron, K. Fridh, M. Hassanzadeh, Concrete alteration due to 55years of exposure to river water: Chemical and mineralogical characterisation, Cement and Concrete Research. 92 (2017) 110–120. https://doi.org/10.1016/j.cemconres.2016.11.012.

[2] K. De Weerdt, E. Bernard, W. Kunther, M.T. Pedersen, B. Lothenbach, Phase changes in cementitious materials exposed to saline solutions, Cement and Concrete Research. 165 (2023) 107071. https://doi.org/10.1016/j.cemconres.2022.107071.

[3] U.H. Jakobsen, K. De Weerdt, M.R. Geiker, Elemental zonation in marine concrete, Cement and Concrete Research. 85 (2016) 12–27. https://doi.org/10.1016/j.cemconres.2016.02.006.

[4] P. Woyciechowski, P. Łukowski, E. Szmigiera, G. Adamczewski, K. Chilmon, S. Spodzieja, Concrete corrosion in a wastewater treatment plant – A comprehensive case study, Construction and Building Materials. 303 (2021) 124388. https://doi.org/10.1016/j.conbuildmat.2021.124388.

[5] A. Leemann, Raman microscopy of alkali-silica reaction (ASR) products formed in concrete, Cement and Concrete Research. 102 (2017) 41–47. https://doi.org/10.1016/j.cemconres.2017.08.014.

[6] J. Lewi, M.G. Minerbe, R. Mailler, M.P. Lavigne, I. Nour, P. Meche, S. Azimi, V. Rocher, T. Chaussadent, Détérioration des matériaux cimentaires dans les ouvrages de nitrification des stations d'épuration, Matériaux & Techniques. 108 (2020) 306. https://doi.org/10.1051/mattech/2020030.

[7] J. Duchesne, A. Bertron, Leaching of Cementitious Materials by Pure Water and Strong Acids (HCl and HNO3), in: M. Alexander, A. Bertron, N. De Belie (Eds.), Performance of Cement-Based Materials in Aggressive Aqueous Environments: State-of-the-Art Report, RILEM TC 211 - PAE, Springer Netherlands, Dordrecht, 2013: pp. 91–112. https://doi.org/10.1007/978-94-007-5413-3_4.

[8] A. Bertron, J. Duchesne, Attack of Cementitious Materials by Organic Acids in Agricultural and Agrofood Effluents, in: M. Alexander, A. Bertron, N. De Belie (Eds.), Performance of Cement-Based Materials in Aggressive Aqueous Environments, Springer, Dordrecht, 2013: pp. 131–173. https://doi.org/10.1007/978-94-007-5413-3_6.

[9] S. Rehacek, D. Dobias, P. Pokorny, D. Citek, J. Kolisko, Issues of Concrete in Silage Pits, IOP Conf. Ser.: Mater. Sci. Eng. 324 (2018) 012023. https://doi.org/10.1088/1757-899X/324/1/012023.

[10] M. Weydert, L. Van Caenegem, P. Dehon, AE—Automation and Emerging Technologies: Resistance of Concrete, Asphaltic Concrete and Mastic

Asphalt to Silage Juice, Journal of Agricultural Engineering Research. 79 (2001) 151–157. https://doi.org/10.1006/jaer.2000.0691.
[11] A. Hubáček, R. Hela, Concrete in the Environment of Agricultural Buildings, Solid State Phenomena. 322 (2021) 35–40. https://doi.org/10.4028/www.scientific.net/SSP.322.35.
[12] A. Bertron, M. Peyre Lavigne, C. Patapy, B. Erable, Biodeterioration of concrete in agricultural, agro-food and biogas plants: state of the art and challenges, RILEM Technical Letters. 2 (2017) 83–89. https://doi.org/10.21809/rilemtechlett.2017.42.
[13] A. Bertron, M. Coutand, X. Cameleyre, G. Escadeillas, J. Duchesne, Attaques chimique et biologique des effluents agricoles et agroalimentaires sur les matériaux cimentaires, Mater. Tech. 93 (2005) s.111-s.121. https://doi.org/10.1051/mattech:2006010.
[14] N. De Belie, On-Farm Trial to Determine the Durability of Different Concrete Slats for Fattening Pigs, Journal of Agricultural Engineering Research. 68 (1997) 311–316. https://doi.org/10.1006/jaer.1997.0209.
[15] N. De Belie, J.J. Lenehan, C.R. Braam, B. Svennerstedt, M. Richardson, B. Sonck, Durability of Building Materials and Components in the Agricultural Environment, Part III: Concrete Structures, Journal of Agricultural Engineering Research. 76 (2000) 3–16. https://doi.org/10.1006/jaer.1999.0520.
[16] C. O'Donnell, V.A. Dodd, P. O'Kiely, M. Richardson, A Study of the Effects of Silage Effluent on Concrete: Part 1, Significance of Concrete Characteristics, Journal of Agricultural Engineering Research. 60 (1995) 83–92. https://doi.org/10.1006/jaer.1995.1002.
[17] M. Giroudon, C. Patapy, M. Peyre Lavigne, M. Andriamiandroso, R. Cartier, S. Dubos, C. Bacquié, L. André, S. Pommier, X. Lefevbre, M. Cyr, A. Bertron, Potential of low carbon materials facing biodeterioration in concrete biogas structures, Mater Struct. 56 (2023) 80. https://doi.org/10.1617/s11527-023-02174-0.
[18] M. Giroudon, C. Perez, M. Peyre Lavigne, B. Erable, C. Lors, C. Patapy, A. Bertron, Insights into the local interaction mechanisms between fermenting broken maize and various binder materials for anaerobic digester structures, Journal of Environmental Management. 300 (2021) 113735. https://doi.org/10.1016/j.jenvman.2021.113735.
[19] M. Giroudon, M. Peyre Lavigne, C. Patapy, A. Bertron, Blast-furnace slag cement and metakaolin based geopolymer as construction materials for liquid anaerobic digestion structures: Interactions and biodeterioration mechanisms, Science of The Total Environment. 750 (2021) 141518. https://doi.org/10.1016/j.scitotenv.2020.141518.

[20] C. Voegel, M. Giroudon, A. Bertron, C. Patapy, M. Peyre Lavigne, T. Verdier, B. Erable, Cementitious materials in biogas systems: Biodeterioration mechanisms and kinetics in CEM I and CAC based materials, Cement and Concrete Research. 124 (2019) 105815. https://doi.org/10.1016/j.cemconres.2019.105815.
[21] A. Bertron, J. Duchesne, G. Escadeillas, Accelerated tests of hardened cement pastes alteration by organic acids: analysis of the pH effect, Cement and Concrete Research. 35 (2005) 155–166. https://doi.org/10.1016/j.cemconres.2004.09.009.
[22] M. Alexander, A. Bertron, N. De Belie, eds., Performance of Cement-Based Materials in Aggressive Aqueous Environments: State-of-the-Art Report, RILEM TC 211 - PAE, Springer Netherlands, Dordrecht, 2013. https://doi.org/10.1007/978-94-007-5413-3.
[23] M. Giroudon, M. Peyre Lavigne, C. Patapy, A. Bertron, Laboratory assessment of the contribution of aggressive to concrete chemical compounds to the degradation of Portland cement-based materials during anaerobic digestion, Mater Struct. 54 (2021) 218. https://doi.org/10.1617/s11527-021-01810-x.
[24] B. Lothenbach, D.A. Kulik, T. Matschei, M. Balonis, L. Baquerizo, B. Dilnesa, G.D. Miron, R.J. Myers, Cemdata18: A chemical thermodynamic database for hydrated Portland cements and alkali-activated materials, Cement and Concrete Research. 115 (2019) 472–506. https://doi.org/10.1016/j.cemconres.2018.04.018.
[25] Ph. Blanc, A. Lassin, P. Piantone, M. Azaroual, N. Jacquemet, A. Fabbri, E.C. Gaucher, Thermoddem: A geochemical database focused on low temperature water/rock interactions and waste materials, Applied Geochemistry. 27 (2012) 2107–2116. https://doi.org/10.1016/j.apgeochem.2012.06.002.
[26] J.P. Gustafsson, Visual MINTEQ version 3.0. KTH, in: Department of Land and Water Resources Engineering, Stockolm, Sweden, 2010.
[27] X. Ke, S.A. Bernal, J.L. Provis, B. Lothenbach, Thermodynamic modelling of phase evolution in alkali-activated slag cements exposed to carbon dioxide, Cement and Concrete Research. 136 (2020) 106158. https://doi.org/10.1016/j.cemconres.2020.106158.
[28] B. Walkley, X. Ke, O. Hussein, J. L. Provis, Thermodynamic properties of sodium aluminosilicate hydrate (N–A–S–H), Dalton Transactions. 50 (2021) 13968–13984. https://doi.org/10.1039/D1DT02202D.
[29] R.J. Myers, B. Lothenbach, S.A. Bernal, J.L. Provis, Thermodynamic modelling of alkali-activated slag cements, Applied Geochemistry. 61 (2015) 233–247. https://doi.org/10.1016/j.apgeochem.2015.06.006.

[30] F. Berger, A. Bogner, A. Hirsch, N. Ukrainczyk, F. Dehn, E. Koenders, Thermodynamic Modeling and Experimental Validation of Acetic Acid Attack on Hardened Cement Paste: Effect of Silica Fume, Materials. 15 (2022) 8355. https://doi.org/10.3390/ma15238355.
[31] A. Bertron, J. Duchesne, G. Escadeillas, Attack of cement pastes exposed to organic acids in manure, Cement and Concrete Composites. 27 (2005) 898–909. https://doi.org/10.1016/j.cemconcomp.2005.06.003.
[32] AFNOR, NF EN 196-1. Methods of testing cement - Part 1: Determination of strength, Paris, France, 2016.
[33] K. Scrivener, R. Snellings, B. Lothenbach, A Practical Guide to Microstructural Analysis of Cementitious Materials, CRC Press, 2016.
[34] R. Snellings, J. Chwast, Ö. Cizer, N. De Belie, Y. Dhandapani, P. Durdzinski, J. Elsen, J. Haufe, D. Hooton, C. Patapy, M. Santhanam, K. Scrivener, D. Snoeck, L. Steger, S. Tongbo, A. Vollpracht, F. Winnefeld, B. Lothenbach, RILEM TC-238 SCM recommendation on hydration stoppage by solvent exchange for the study of hydrate assemblages, Mater Struct. 51 (2018) 172. https://doi.org/10.1617/s11527-018-1298-5.
[35] M. Thompson, J.N. Walsh, Inductively coupled plasma mass spectrometry, in: Handbook of Inductively Coupled Plasma Spectrometry: Second Edition, Second Edition, Springer US, Boston, MA, 1989: pp. 238–269.
[36] G. Tyler, ICP-OES, ICP-MS and AAS Techniques Compared, ICP Optical Emission Spectroscopy. (1995) 11.
[37] C. Vandecasteele, C.B. Block, Modern Methods for Trace Element Determination, John Wiley & Sons, 1997.
[38] N.T. Duong, J. Trébosc, O. Lafon, J.-P. Amoureux, Improved sensitivity and quantification for 29Si NMR experiments on solids using UDEFT (Uniform Driven Equilibrium Fourier Transform), Solid State Nuclear Magnetic Resonance. 100 (2019) 52–62. https://doi.org/10.1016/j.ssnmr.2019.03.007.
[39] M. Wojdyr, Fityk: a general-purpose peak fitting program, J Appl Cryst. 43 (2010) 1126–1128. https://doi.org/10.1107/S0021889810030499.
[40] I. Klur, Etude par RMN de la structure des silicates de calcium hydrates, These de doctorat, Paris 6, 1996. https://www.theses.fr/1996PA066213.
[41] J. Skibsted, H.J. Jakobsen, Characterization of the Calcium Silicate and Aluminate Phases in Anhydrous and Hydrated Portland Cements by 27Al and 29Si MAS NMR Spectroscopy, in: P. Colombet, H. Zanni, A.-R. Grimmer, P. Sozzani (Eds.), Nuclear Magnetic Resonance Spectroscopy of Cement-Based Materials, Springer, Berlin, Heidelberg, 1998: pp. 3–45. https://doi.org/10.1007/978-3-642-80432-8_1.

[42] P. Colombet, A.-R. Grimmer, H. Zanni, P. Sozzani, Nuclear Magnetic Resonance Spectroscopy of Cement-Based Materials, Springer Berlin Heidelberg, 1998.
[43] H.C. Helgeson, Thermodynamics of hydrothermal systems at elevated temperatures and pressures, Am J Sci. 267 (1969) 729–804. https://doi.org/10.2475/ajs.267.7.729.
[44] P. Debye, E. Hückel, Zur Theorie der Elektrolyte, Physikalische Zeitschrift. 24 (1923) 185–206.
[45] G.M. Kontogeorgis, B. Maribo-Mogensen, K. Thomsen, The Debye-Hückel theory and its importance in modeling electrolyte solutions, Fluid Phase Equilibria. 462 (2018) 130–152. https://doi.org/10.1016/j.fluid.2018.01.004.
[46] D.L. Parkhurst, C.A.J. Appelo, Description of input and examples for PHREEQC version 3: a computer program for speciation, batch-reaction, one-dimensional transport, and inverse geochemical calculations, in: Modeling Techniques, U.S. Geological Survey, Denver, CO, 2013: p. 497.
[47] G. Möschner, B. Lothenbach, F. Winnefeld, A. Ulrich, R. Figi, R. Kretzschmar, Solid solution between Al-ettringite and Fe-ettringite (Ca6[Al1−xFex(OH)6]2(SO4)3·26H2O), Cement and Concrete Research. 39 (2009) 482–489. https://doi.org/10.1016/j.cemconres.2009.03.001.
[48] B.Z. Dilnesa, B. Lothenbach, G. Le Saout, G. Renaudin, A. Mesbah, Y. Filinchuk, A. Wichser, E. Wieland, Iron in carbonate containing AFm phases, Cement and Concrete Research. 41 (2011) 311–323. https://doi.org/10.1016/j.cemconres.2010.11.017.
[49] B.Z. Dilnesa, B. Lothenbach, G. Renaudin, A. Wichser, E. Wieland, Stability of Monosulfate in the Presence of Iron, Journal of the American Ceramic Society. 95 (2012) 3305–3316. https://doi.org/10.1111/j.1551-2916.2012.05335.x.
[50] B.Z. Dilnesa, E. Wieland, B. Lothenbach, R. Dähn, K.L. Scrivener, Fe-containing phases in hydrated cements, Cement and Concrete Research. 58 (2014) 45–55. https://doi.org/10.1016/j.cemconres.2013.12.012.
[51] B.Z. Dilnesa, B. Lothenbach, G. Renaudin, A. Wichser, D. Kulik, Synthesis and characterization of hydrogarnet Ca3(AlxFe1−x)2(SiO4)y(OH)4(3−y), Cement and Concrete Research. 59 (2014) 96–111. https://doi.org/10.1016/j.cemconres.2014.02.001.
[52] L. De Windt, P. Devillers, Modeling the degradation of Portland cement pastes by biogenic organic acids, Cement and Concrete Research. 40 (2010) 1165–1174. https://doi.org/10.1016/j.cemconres.2010.03.005.
[53] L. De Windt, A. Bertron, S. Larreur-Cayol, G. Escadeillas, Interactions between hydrated cement paste and organic acids: Thermodynamic data

and speciation modeling, Cement and Concrete Research. 69 (2015) 25–36. https://doi.org/10.1016/j.cemconres.2014.12.001.
[54] C. Roosz, P. Vieillard, P. Blanc, S. Gaboreau, H. Gailhanou, D. Braithwaite, V. Montouillout, R. Denoyel, P. Henocq, B. Madé, Thermodynamic properties of C-S-H, C-A-S-H and M-S-H phases: Results from direct measurements and predictive modelling, Applied Geochemistry. 92 (2018) 140–156. https://doi.org/10.1016/j.apgeochem.2018.03.004.
[55] D.L. Parkhurst, C.A.J. Appelo, User's guide to PHREEQC (Version 2) : a computer program for speciation, batch-reaction, one-dimensional transport, and inverse geochemical calculations, in: Water-Resources Investigations Report, DC, 1999. https://doi.org/10.3133/wri994259.
[56] A. Bertron, Methods for Testing Cementitious Materials Exposed to Organic Acids, in: Performance of Cement-Based Materials in Aggressive Aqueous Environments, Springer, Dordrecht, 2013: pp. 355–387.
[57] P. Barret, F.P. Glasser, eds., Chemistry of Cements for Nuclear Applications, Elsevier, 1992.
[58] L. Sánchez, J. Cuevas, S. Ramírez, D. Riuiz De León, R. Fernández, R. Vigil Dela Villa, S. Leguey, Reaction kinetics of FEBEX bentonite in hyperalkaline conditions resembling the cement–bentonite interface, Applied Clay Science. 33 (2006) 125–141. https://doi.org/10.1016/j.clay.2006.04.008.
[59] M. Fukuhara, S. Goto, K. Asaga, M. Daimon, R. Kondo, Mechanisms and kinetics of C4AF hydration with gypsum, Cement and Concrete Research. 11 (1981) 407–414. https://doi.org/10.1016/0008-8846(81)90112-5.
[60] C. Plowman, J.G. Cabrera, Mechanism and kinetics of hydration of C3A and C4AF. Extracted from cement, Cement and Concrete Research. 14 (1984) 238–248. https://doi.org/10.1016/0008-8846(84)90110-8.
[61] J. Rose, A. Bénard, S. El Mrabet, A. Masion, I. Moulin, V. Briois, L. Olivi, J.-Y. Bottero, Evolution of iron speciation during hydration of C4AF, Waste Management. 26 (2006) 720–724. https://doi.org/10.1016/j.wasman.2006.01.021.
[62] A. Bertron, J. Duchesne, G. Escadeillas, Degradation of cement pastes by organic acids, Mater Struct. 40 (2007) 341–354. https://doi.org/10.1617/s11527-006-9110-3.
[63] X. Cong, R.J. Kirkpatrick, 29Si MAS NMR study of the structure of calcium silicate hydrate, Advanced Cement Based Materials. 3 (1996) 144–156. https://doi.org/10.1016/S1065-7355(96)90046-2.
[64] K. Garbev, G. Beuchle, M. Bornefeld, L. Black, P. Stemmermann, Cell Dimensions and Composition of Nanocrystalline Calcium Silicate Hydrate Solid Solutions. Part 1: Synchrotron-Based X-Ray Diffraction, Journal of

the American Ceramic Society. 91 (2008) 3005–3014. https://doi.org/10.1111/j.1551-2916.2008.02484.x.
[65] K. Garbev, M. Bornefeld, G. Beuchle, P. Stemmermann, Cell Dimensions and Composition of Nanocrystalline Calcium Silicate Hydrate Solid Solutions. Part 2: X-Ray and Thermogravimetry Study, Journal of the American Ceramic Society. 91 (2008) 3015–3023. https://doi.org/10.1111/j.1551-2916.2008.02601.x.
[66] S. Grangeon, F. Claret, C. Roosz, T. Sato, S. Gaboreau, Y. Linard, Structure of nanocrystalline calcium silicate hydrates: insights from X-ray diffraction, synchrotron X-ray absorption and nuclear magnetic resonance, J Appl Cryst. 49 (2016) 771–783. https://doi.org/10.1107/S1600576716003885.
[67] S. Grangeon, F. Claret, Y. Linard, C. Chiaberge, X-ray diffraction: a powerful tool to probe and understand the structure of nanocrystalline calcium silicate hydrates, Acta Cryst B. 69 (2013) 465–473. https://doi.org/10.1107/S2052519213021155.
[68] M.D. Andersen, H.J. Jakobsen, J. Skibsted, Incorporation of Aluminum in the Calcium Silicate Hydrate (C−S−H) of Hydrated Portland Cements: A High-Field 27Al and 29Si MAS NMR Investigation, Inorg. Chem. 42 (2003) 2280–2287. https://doi.org/10.1021/ic020607b.
[69] P. Faucon, F. Adenot, J.F. Jacquinot, J.C. Petit, R. Cabrillac, M. Jorda, Long-term behaviour of cement pastes used for nuclear waste disposal: review of physico-chemical mechanisms of water degradation, Cement and Concrete Research. 28 (1998) 847–857. https://doi.org/10.1016/S0008-8846(98)00053-2.
[70] M.D. Andersen, H.J. Jakobsen, J. Skibsted, A new aluminium-hydrate species in hydrated Portland cements characterized by 27Al and 29Si MAS NMR spectroscopy, Cement and Concrete Research. 36 (2006) 3–17. https://doi.org/10.1016/j.cemconres.2005.04.010.
[71] H.F.W. Taylor, Hydrated calcium silicates. Part I. Compound formation at ordinary temperatures, J. Chem. Soc. (1950) 3682–3690. https://doi.org/10.1039/JR9500003682.
[72] P. Henocq, A sorption model for alkalis in cement-based materials – Correlations with solubility and electrokinetic properties, Physics and Chemistry of the Earth, Parts A/B/C. 99 (2017) 184–193. https://doi.org/10.1016/j.pce.2017.05.004.
[73] A. Bertron, G. Escadeillas, J. Duchesne, Cement pastes alteration by liquid manure organic acids: chemical and mineralogical characterization, Cement and Concrete Research. 34 (2004) 1823–1835. https://doi.org/10.1016/j.cemconres.2004.01.002.

[74] B. Walkley, R. San Nicolas, M.-A. Sani, G.J. Rees, J.V. Hanna, J.S.J. van Deventer, J.L. Provis, Phase evolution of C-(N)-A-S-H/N-A-S-H gel blends investigated via alkali-activation of synthetic calcium aluminosilicate precursors, Cement and Concrete Research. 89 (2016) 120–135. https://doi.org/10.1016/j.cemconres.2016.08.010.
[75] R.J. Myers, S.A. Bernal, J.L. Provis, A thermodynamic model for C-(N-)A-S-H gel: CNASH_ss. Derivation and validation, Cement and Concrete Research. 66 (2014) 27–47. https://doi.org/10.1016/j.cemconres.2014.07.005.
[76] E.C. Gaucher, P. Blanc, Cement/clay interactions – A review: Experiments, natural analogues, and modeling, Waste Management. 26 (2006) 776–788. https://doi.org/10.1016/j.wasman.2006.01.027.
[77] R. Mathieu, P. Vieillard, A predictive model for the enthalpies of formation of zeolites, Microporous and Mesoporous Materials. 132 (2010) 335–351. https://doi.org/10.1016/j.micromeso.2010.03.011.